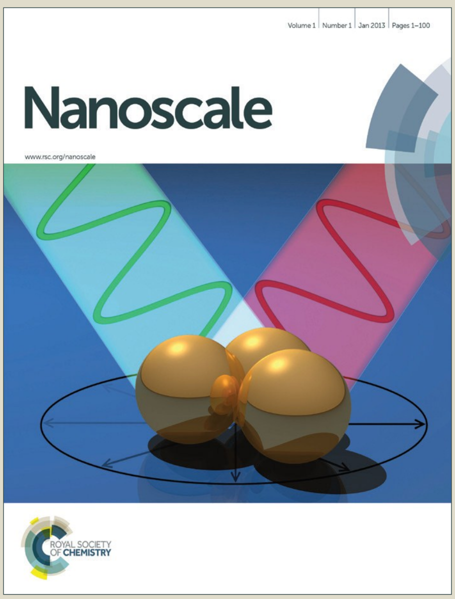
Nanoscale
ROYAL SOCIETY OF CHEMISTRY

Discovery of Elusive Structures of Multifunctional Transition-Metal Borides

Yongcheng Liang,*[a] Zhaobing Wu,[a] Xun Yuan,[ab] Wenqing Zhang*[bc] and Peihong Zhang*[cd]

[a]*College of Engineering Science and Technology, Shanghai Ocean University, Shanghai 201306, China*

[b]*State Key Laboratory of High Performance Ceramics and Superfine Microstructures, Shanghai Institute of Ceramics, Chinese Academy of Sciences, Shanghai 200050, China*

[c]*Materials Genome Institute and Department of Physics, Shanghai University, Shanghai 200444, China*

[d]*Department of Physics, University at Buffalo, State University of New York, Buffalo, New York 14260, USA*

*ycliang@shou.edu.cn, wqzhang@mail.sic.ac.cn, pzhang3@buffalo.edu

A definitive determination of crystal structures is an important prerequisite for designing and exploiting new functional materials. Even though tungsten and molybdenum borides (TMB_x) are the prototype for transition-metal light-element compounds with multiple functionalities, their elusive crystal structures have puzzled scientists for decades. Here, we discover that the long-assumed TMB_2 phases with the simple *hP*3 structure (*hP*3-TMB_2) are in fact a family of complex TMB_3 polytypes with a nanoscale ordering along the axial direction. Compared with the energetically unfavorable and dynamically unstable *hP*3-TMB_2 phase, the energetically more favorable and dynamically stable TMB_3 polytypes better explain the experimental structural parameters, mechanical properties, and X-ray diffraction (XRD) patterns. We demonstrate that such a structural and compositional modification from the *hP*3-TMB_2 phases to the TMB_3 polytypes originates from the relief of the strong antibonding interaction between *d* electrons by removing one third of metal atoms systematically. These results resolve the longstanding structural mystery of this class of metal borides and uncover a hidden family of polytypic structures. Moreover, these polytypic structures provides additional hardening mechanism by forming nanoscale interlocks that may strongly hinder the interlayer sliding movements, which promises to open a new avenue towards designing novel superhard nanocomposite materials by exploiting the coexistence of various polytypes.

1. Introduction

Transition-metal borides have been of tremendous interest to researchers in both fundamental materials science and technological applications due to their unique mechanical, electronic and magnetic properties.[1-13] Nevertheless, the structural and compositional uncertainties of these materials have impeded an in-depth understanding of their properties and thus their potential usage. The involvement of heavy transition-metal atoms hampers the accuracy of locating light boron atoms in XRD experiments. Furthermore, the versatile abilities of boron atoms to form *sp*-, sp^2-, and sp^3-hybridized bonds bring about the coexistence of miscellaneous phases during synthesis,[14, 15] and this situation is exacerbated by the presence of excess boron that is strongly adhered to the crystallites, leading to formidable interferences when one attempts to interpret X-ray and neutron diffraction data. These technological challenges have contributed to significant uncertainties in the structural and compositional characterizations of these materials.

The simple *hP*3 structure (i.e., the AlB_2 structure, space group *P*6/*mmm*) has been widely accepted as a primary structure for diborides of many transition metals (e.g., from Sc to Mn in the 3*d* series, from Y to Mo in the 4*d* series, and from Lu to W in the 5*d* series).[16, 17] Among them, the presumed *hP*3-WB_2 phase has recently attracted renewed attention due to its extraordinary properties and functionalities (e.g., high hardness, high melting point, chemical inertness, and facile ambient-pressure synthesis). Although novel multifunctionality has been discovered in such a well-known and accessible binary system, its precise crystal structure is a subject of increasing controversy. In 1966, the synthesis of *hP*3-WB_2 was first reported.[18] Nevertheless, recent theoretical works questioned its existence at ambient conditions and concluded that it should be a high-pressure phase above 65 GPa by calculating relative energies of several competing phases [i.e., *hP*6 (space group $P6_3/mmc$), *hP*12 (space group $P6_3/mmc$), *oP*6 (space group *Pmmn*)].[19, 20] A more recent study, however, reveals that the *hR*18 structure (space group *R*-3*m*) is more stable than the *hP*3 structure below 100 GPa, ruling out the possibility of *hP*3-WB_2 being a high-pressure phase below 100 GPa.[21] Later, first-principles calculations further questioned the existence of *hP*3-WB_2 based on the study of its thermodynamic and dynamical properties.[22, 23] Interestingly, a new metastable *hR*9-WB_2 phase (space group *R*-3*m*) was predicted by means of structural evolutionary algorithms.[24, 25] Meanwhile, Frotscher *et al*.[26] tried but failed to synthesize *hP*3-WB_2, but they concluded that previously established *hP*14-W_2B_5 should be *hP*12-WB_2. Hayami *et al*.[27] investigated the effect of boron defects on the synthesizability of *hP*3-WB_2. Although their calculations showed that *hP*3-WB_2 became minimally stable with some boron vacancies added, they failed to find any trace of *hP*3-WB_{2-x}. Thus they concluded that *hP*3-WB_{2-x} may not actually exist in the W-B binary system. In spite of these doubts, the most recent experiment surprisingly reported that *hP*3-WB_2 has again been synthesized by the dc magnetron sputtering technique. Moreover, its nanocomposite coatings exhibit outstanding properties (e.g., superhardness, good thermal conductivity).[28, 29] This most recent experiment, together with earlier theoretical and experimental efforts, strongly suggests that there is an unknown stable phase of tungsten boride which may be closely related to the *hP*3 structure, but fundamentally different from the already identified structures (i.e., *hP*6, *hP*12, *hR*18, *hR*9, *oP*6). Since molybdenum is isoelectronic with tungsten, the *hP*3 structure of MoB_2 has similarly faced an unabated debate. A number of experiments reported its synthesis,[30-33] whereas theoretical studies were skeptical of its existence.[34, 35] These seemingly contradictory results greatly limit the understanding of structure-property relationships for this class of materials and thus hinder new developments in this field. Until now, the fundamental structures of these materials have never been fully resolved, and it is likely that a family of unidentified structures is hidden in these transition-metal borides.

On the other hand, the highest boride of tungsten has currently been recognized as a promising superhard material.[36-43] However, this nominal WB_4 with the *hP*20 structure[44] has been modified as stoichiometric WB_3 with the *hP*16 structure (space group $P6_3/mmc$) by recent theoretical and experimental works.[21, 24, 25, 45-50] Its ground-state *hR*24 structure (space group *R*-3*m*) has subsequently been uncovered theoretically.[22-25, 48] In addition, previously assumed *hP*20-MoB_4 was later determined to be *hP*16-MoB_3,[35, 46, 51] and *hR*24-MoB_3 was also predicted.[25, 34, 35] By applying the stacking principle of the two basic structures, *hP*16 and *hR*24, polytypism has been revealed as the extra degree of freedom in the structure design of TMB_3, which produces a large number of polytypic phases with different stacking patterns of metal layers.[52] More interestingly, this polytypism may result in the coexistence of superhardness and anomalously low lattice thermal conductivity in TMB_3, which promises to open a new avenue to designing superhard materials with additional functionalities. Unfortunately, the electronic origins for the formation and stability for the polytypic structures have not been clearly explained. In particular, it is still unknown whether these theoretically identified TMB_3 polytypes correlate with the experimentally claimed *hP*3-TMB_2 phases.

In this article, by means of density functional theory (DFT) calculations in comparison with the available experimental data, we comprehensively investigate the W-B and Mo-B systems aiming at resolving the aforementioned apparent discrepancy between experiment and theory. We discover that the long perceived *hP*3-TMB_2 phases are actually a misinterpretation for a family of more complicated MB_3 polytypes with a nanoscale ordering along the axial direction. The former are energetically unfavorable and dynamically unstable, and their structural parameters, mechanical properties and XRD deviate significantly from experiments. In contrast, the latter are energetically more favorable and dynamically stable, and their corresponding properties agree well with experiments. Equally importantly, we provide a clear explanation of the electronic origins of such a structural and compositional modification from the *hP*3-TMB_2 phases to the TMB_3 polytypes. The present results not only rectify previous incorrect structural assignments, but also discover a hidden family of polytypes that promise to create novel superhard nanocomposite materials with multiple functionalities.

2 Methods

The behaviors of the W-B and Mo-B systems are investigated using all-electron projector augmented wave (PAW) method with $5d^46s^2$, $4d^45s^2$ and $2s^22p^1$ electrons as valences for W, Mo and B, respectively, as implemented in the VASP code.[53] The exchange-correlation functional within the generalized gradient approximation (GGA)[54] is employed. A plane-wave basis set with a large cutoff energy of 500 eV and the Monkhorst-Pack *k*-mesh with a dense grid of 0.02 $Å^{-1}$ are adopted for the considered phases to ensure that the numerical accuracy be able to resolve an energy difference of less than 1 meV/atom. Forces on the ions are calculated through the Hellmann-Feynman theorem, allowing a full geometry optimization for all studied structures.

The phonon dispersions are calculated using the PHONOPY package[55] based on a supercell approach, and we use the VASP code to calculate the force constants. The mechanical properties (elastic constants, bulk modulus, shear modulus, Young's modulus and Possion's ratio) were determined by an efficient strain-energy method[56] while the Vickers hardness was estimated by Chen's model.[57, 58]

3 Results and discussion

We reexamine the energetic and dynamical stability of the *hP*3 structure and other candidate structures (i.e., *hP*6, *hP*12, *hR*18, *hR*9, *oP*6) for TMB_2. The total energies of WB_2 and MoB_2 as a function of volumes for various structures are depicted in Fig. 1(a) and 1(b), respectively. For WB_2 (MoB_2), the *hP*6 (*hR*18) structure has the lowest energy among the six candidates. It is rather surprising that the long assumed *hP*3 structure is the most energetically unfavorable with 0.847 eV/formula (0.465 eV/formula) higher than the *hP*6 (*hR*18) structure at their respective equilibrium volumes. With such a large energy difference, it is unlikely that temperature effects could stabilize the *hP*3 structure. The phonon dispersion curves for *hP*3-WB_2 and *hP*3-MoB_2 are shown in Fig. 1(c) and 1(d), respectively. A multitude of unstable phonon modes with very large imaginary frequencies clearly rules out the *hP*3 structure as a possible phase for WB_2 (MoB_2). These results confirm that *hP*3-WB_2 and *hP*3-MoB_2 are unstable and are consistent with recent theoretical works.[22-25, 34, 35] In contrast, other five competitive structures (i.e., *hP*6, *hP*12, *hR*18, *hR*9, *oP*6) not only have significantly lower energies but also are dynamically stable (see their respective phonon dispersions shown in Fig. 2), supporting the recent theoretical and experimental conclusions.[19-27, 59] The real puzzle is why the obviously unstable phases (*hP*3-TMB_2) seem to show up experimentally.[18, 26-33] The most plausible explanation is that what were observed experimentally are not the *hP*3 structure, but structures that are closely related to *hP*3. These *hP*3-like structures are energetically competitive but distinct from all of the above stable phases.

It is rather puzzling that W-B and Mo-B systems do not follow the general structural trend of other transition-metal diborides. This naturally raises the following fundamental questions: (a) Why can't the W-B and Mo-B systems assume the *hP*3 structure as many other transition-metal diborides do? (b) What are the real composition and stable structures of the wrongly assumed *hP*3-TMB_2 phases, and do they correlate with the recently proposed TMB_3 polytypes? (c) Whether are these TMB_3 polytypes stable, and can they explain the experimental observations?

As shown in Fig. 3(a), boron atoms form rigid graphitelike hexagonal (H) sheets in *hP*3-TMB_2. Metal atoms sit directly in the interstices above and below the centers of boron hexagons and form close-packed metal (M) layers. Considering that this structure is unstable for WB_2 and MoB_2 but is stable for many other transition-metal diborides, it is of great interest to understand the electronic origins of this structural instability. As an illustrative case, the total density of states (DOS), B-projected DOS, W-projected DOS, and band structure of *hP*3-WB_2 are presented in Fig. 4(a), 4(b), 4(c), and 4(d), respectively. The chemical bonding mechanism of *hP*3-WB_2 can be understood as follows: First, in the boron layer, the interaction between two boron atoms results in the formation of three bonding and three antibonding B-2sp^2 hybridized orbitals, leaving two nonbonding 2p_z orbitals. Second, upon adding one tungsten atom to the boron framework to form *hP*3-WB_2, each metal atom has a hexagonal prismatic boron environment. This local environment breaks the degeneracy of W-5*d* orbitals, forming three types of orbitals, namely, degenerate 5d_{xy} and 5$d_{x^2-y^2}$, degenerate 5d_{yz} and 5d_{xz}, and 5d_{z^2}. Since the W-5*d* states lie very close in energy to the B-2*sp* states, there is a strong hybridization among these states. Our calculated DOS and band structures confirm this chemical bonding picture. The lowest five bands in the range of (-16, -3) eV can be viewed as the bonding states of the W-B hybridization, among which the lower three (upper two) bands are mainly derived from the degenerate 5d_{xy} and 5$d_{x^2-y^2}$ (5d_{yz} and 5d_{xz}) states and the B-2sp^2 bonding (B-2p_z nonbonding) states, while the region above -3 eV is the corresponding antibonding part.

This analysis naturally leads to the conclusion that the most stable valence-electron concentration (VEC) of the *hP*3 structure should be 10 electrons/formula. In other words, the *hP*3 structure shows the highest stability when the five bonding bands are completely filled. If VEC decreases to below 10 electrons/formula, the bonding states are partially filled, giving rise to a negative contribution to the stability; if VEC increases to above 10 electrons/formula, the antibonding states start to be populated, also leading to a negative contribution to the stability. For WB_2, the VEC is 12 electrons/formula and the sixth band is substantially filled. As highlighted in red in Fig. 4(c) and 4(d), the sixth band ranging from -3 to 1 eV is mainly derived from the antibonding W-5d_{z^2} states. A study on crystal orbital overlap population (COOP) for a series of metal diborides has shown that this antibonding orbital is controlled by the direct metal-metal interaction perpendicular to the boron layers.[60] It is this strong antibonding interaction that is responsible for the instability of *hP*3-WB_2. The same argument can be applied for *hP*3-MoB_2. These results capture the nature of the instability of *hP*3-TMB_2, and explain the experimentally observed trends of cohesive-energy related properties for this class of diborides. For example, the melting temperature and formation heat show a maximum at TiB_2 among the first-row transition-metal diborides, and they smoothly decrease as VEC deviates from 10 electrons/formula.[61, 62]

Therefore, it is clear that the metal d_z^2 antibonding states are responsible for the instability of *hP*3-TMB_2. If the occupation of these unfavorable antibonding states could be reduced or eliminated, the stability may be restored. As a matter of fact, the aforementioned competitive structures (i.e., *hP*6, *hP*12, *hR*18, *hR*9, *oP*6) are a result of different structural distortions to the *hP*3 structure. For example, the *hP*12 structure is derived from the *hP*3 structure by translating double metal layers with respect to each other so as to stagger the metal atom along the *c*-axial direction, while puckering boron layers between the staggered metal layers so that the close TM-B distances remain. This type of structural modifications is an effective way of reducing the antibonding interaction, as confirmed by recent electronic structure calculations.[23, 35] In particular, *hP*12-WB_2 and *hR*18-MoB_2 have been observed experimentally.[26, 59] However, these alternative phases cannot explain the observations of *hP*3-like structures in experiment, and there must be other structural stabilization mechanism that does not significantly modified the *hP*3 structure.

One such mechanism is through the formation of metal-deficient structures (i.e., $TM_{1-x}B_2$) based on the *hP*3 structure. According to the 10-electron VEC rule, the most stable metal-deficient structure would be $TM_{2/3}B_2$ (i.e., TMB_3) with the methodical removal of one-third of metal atoms from the *hP*3 structure as shown in Fig. 3(b). Depending on the stacking sequence of metal-deficient layers, one can construct various stable structures. For example, the experimentally observed *hP*16 (or the theoretically predicted *hR*24) of TMB_3 can be understood as the AHBH (or AHBHCH) (here A, B, and C denote metal layers with one-third vacancies and H is the hexagonal boron layer) stacking sequence of the metal-deficient $TM_{2/3}B_2$ structure. Other TMB_3 polytypes (e.g., AHBHAHCH, AHBHAHBHCH, etc.) can be constructed this way. Hence, this family of polytypic structures consist of identical units of substructure (AH), piled one on top of the other in different numbers and in different stacking orders within the unit cells, but all can be regarded as the metal-deficient *hP*3 structures. We would like to emphasize that in this family of polytypic structures, the vacancy is ordered in the metal layers, skipping one column in every three [see Fig. 3(b)], but the stacking of metal layers may be rather random since different stacking patterns are essentially degenerate. Similar to other polytypic crystals (e.g., SiC, CdI_2, ZnS),[63] the TMB_3 polytypes often show the feature of a nanoscale order but a long-range disorder along the one-dimensional stacking direction.

The thermodynamic and dynamical stability of the *hP*3-derived TMB_3 polytypes is further confirmed by our first-principles calculations. We consider a ($\sqrt{3}\times\sqrt{3}\times 3$) supercell of the *hP*3 structure and calculate the vacancy dependence of the formation energy defined as $\Delta E = E(\mathrm{TMB}_y) - E(\mathrm{TM}) - yE(\mathrm{B})$, where the energies E for W (Mo) and B are calculated based on the body-centered cubic tungsten (molybdenum) and alpha rhombohedral boron, respectively. The formation energy of the supercell *hP*3-$TM_{9-x}B_{18}$ as a function of the number of vacancies is presented in Fig. 5. The formation energy of *hP*3-TMB_2 is found to be the relatively high, though it is still negative (-0.249 eV/formula for *hP*3-WB_2 or -0.869 eV/formula for *hP*3-MoB_2). With the gradual removal of metal atoms, the formation energy decreases continuously, indicating increased stability, before hitting x=3. At x=3, *hP*3-$TM_{9-x}B_{18}$ has the lowest formation energy. This structure corresponds to the earlier identified *hR*24-TMB_3 phase. When more metal atoms are removed, the formation energy then rises sharply. We further calculate formation energies of various *hP*3-derived TMB_3 polytypes. All the TMB_3 polytypes have very low formation energies that lie in between the *hP*16 structure (-1.185 eV/formula for WB_3 and -1.256 eV/formula for MoB_3) and the *hR*24 structure (-1.222 eV/formula for WB_3 and -1.283 eV/formula for MoB_3). Thus the energy differences among these polytypes are extremely small and they are all thermodynamically viable. Remarkably, such a structural and compositional modification (from *hP*3-TMB_2 to TMB_3) also completely removes the dynamical instability of *hP*3-TMB_2 discussed earlier [see Fig. 1(c)]. As shown in Fig. 6, the phonon dispersion curves of the *hP*16 and *hR*24 structures have no imaginary frequencies. Since other TMB_3 polytypes are derived from these two basic structures, they are also dynamically stable.

The mechanism for the stabilization of the TMB_3 polytypes can be further substantiated by comparing their electronic structures with *hP*3-TMB_2. As an illustrative example, the total DOS, B-projected DOS, W-projected DOS, and band structure of *hR*24-WB_3 are displayed in Fig. 4(e), 4(f), 4(g), and 4(h), respectively. Since *hR*24-WB_3 is one of the metal-deficient *hP*3-$W_{1-x}B_2$ phase at x=1/3, exactly corresponding to VEC=10 electrons per $W_{2/3}B_2$ formula, the bonding states are fully filled while leaving the strong antibonding states of the W-5d_z^2 orbitals unoccupied. Meanwhile, the Fermi level shifts to the minimum position of DOS. This stabilization mechanism is true for other TMB_3 polytypes. Although different polytypic TMB_3 structures have subtle differences in the stacking sequence, they all share the same B-B and TM-B local environments, and the stacking sequence does not significantly affect the behavior of the TM-d_z^2 antibonding states discussed earlier. As a result, the different polytypic TMB_3 structures are nearly degenerate, and the random stacking of metal layers often occurs. This is the fundamental reason behind polytypism in TMB_3 and explains the difficulties and confusion in characterizing this class of structures.

Our results unambiguously exclude the *hP*3 structure as the possible stable phase for TMB_2 and the derivative TMB_3 polytypes should be experimentally accessible according to their energetic, dynamical and electronic stabilities. It is very likely that the experimentally assumed *hP*3-TMB_2 samples[18, 26-33] are actually the TMB_3 polytypes identified here. More concrete evidence that our assignment is correct comes from the calculated lattice parameters. As listed in Table 1, the relaxed intralayer distances D_1 and interlayer distances D_2 between the nearest-neighbor metal atoms in TMB_3 are compatible with the experimental data within a maximum error of 3%. Although the calculated D_1 for *hP*3-TMB_2 agree with the measured results within an error of 0.4%, their calculated D_2 are much larger (above 10%) than experiments. This is because the filling of the "extra" metal atoms results in a strong antibonding interaction along the *c*-axial direction.

Another compelling support of this conclusion is the large difference in mechanical properties calculated for *hP*3-TMB_2 and the TMB_3 polytypes. Mechanical properties of different WB_3 polytypes are very similar and are hardly affected by the different stacking sequence of metal layers. Interestingly, a drastic hardening of the mechanical properties is observed accompanying such the structural modification from *hP*3-WB_2 to the WB_3 polytypes. The shear modulus is the most important parameters indirectly governing the indentation hardness. The WB_3 polytypes have very high shear modulus (250-252 GPa), which are consistent with the experimentally reported value (249 GPa) of the *hP*16 structure.[41] However, the shear modulus of *hP*3-WB_2 (153 GPa) is very low. This value not only approaches the shear modulus of the pure metal W (150 GPa)[47] but also is only 60% of that for the WB_3 polytypes. Moreover, the elastic constant C_{44} drastically decreases from 277-279 GPa for the WB_3 polytypes to 134 GPa for *hP*3-WB_2, which is consistent with the violent reduction of the shear modulus. A small Poisson's ratio usually indicates directional bonding in a material, which limits the motion of dislocations and thus enhances a material's hardness. The Poisson's ratios of the WB_3 polytypes are in a typical range of 0.168-0.173 for hard and superhard materials such as ReB_2 (0.171) and *c*BN (0.124),[64] but that of *hP*3-WB_2 is 0.301, even larger than that of pure metal W (0.293).[47]

The sharp enhancement of these mechanical properties will most probably be reflected in a variation of the hardness from *hP*3-WB_2 to the WB_3 polytypes, thus we further estimate their Vickers hardness in comparison with the available experimental hardness. Since the sample purity, indentation loads and measured methods are different, the experimentally reported hardness values are quite scattered (31.8-46.2 GPa of WB_4 under the loads of 0.49-4.9 N,[36] 28.1-43.3 GPa of WB_4 under the loads of 0.49-4.9 N,[38] 36.7 GPa of WB_{3+x} under the load of 1 N,[48] 25.5-42.0 GPa of $W_{1-x}B_3$ under the loads of 0.098-4.90 N,[50] 34.6-49.8 GPa of the claimed *hP*3-WB_2 phase with the nanoindentation method[28]). According to Chen's model,[57, 58] the WB_3 polytypes are predicted to possess high intrinsic hardness (38.0-39.4 GPa), which well falls in the range of these measurements. On the contrary, *hP*3-WB_2 is predicted to have a very low hardness (12.2 GPa), which clearly does not agree with experiments. Such a large variation of hardness has its electronic origin. In these layered WB_x structures, the interlayer W-B bonds are relatively weaker than the intralayer B-B bonds, so the intrinsic hardness mainly depends on the interaction between metal and boron layers. For polytypic WB_3 structures, the covalent honeycomb boron layers are interconnected with the zigzag directional W-B chains along the *c*-axial direction, forming a three-dimensional rigid framework. It is this three-dimensional stiff network that is responsible for the high hardness.[23, 47] Upon incorporating extra tungsten atoms into vacancy sites of WB_3 to form $hP3$-WB_2, the filling of the antibonding states W-5d_z^2 results in an increase of the interlayer W-B distances, resulting in a drastic reduction of interlayer agglutinating power. These weakened interlayer interactions allow the metal and boron layers of $hP3$-WB_2 to cleave readily by shear stresses and thus reduce greatly its hardness. Likewise, a drastic hardening from the $hP3$-MoB_2 phase to the MoB_3 polytypes well explains the high hardness of the experimental samples.[33]

We turn to compare the simulated XRD patterns of $hP3$-TMB_2 and TMB_3 with the available experiments. Although a large number of the TMB_3 polytypes can be constructed theoretically, the formation of specific polytypes depends on their relative stability and growth conditions (temperature, pressure, synthesis methods, etc.). It is very difficult to predict precisely which phase is more likely to form under realistic experimental conditions. It is well known that the $hP16$-WB_3 is a high temperature phase,[48] thus it is more easily observed with high-temperature synthesis (the experimentally claimed WB_4, WB_{3+x} or $W_{1-x}B_3$)[36, 38-44, 48, 50]. The calculated XRD of $hP16$-WB_3 agree well with the observed XRD of nominal WB_4,[38] and this has been confirmed by recent theoretical works.[22, 46]

However, the $hP16$-WB_3 phase cannot explain the XRD of the experimentally claimed WB_2 samples.[28] It is well known that synthetic coalescence is very common in most polytypic compounds (e.g., SiC, CdI_2, ZnS),[63]. Moreover, different WB_3 polytypes are energetically nearly degenerate, thus it is very likely that multiple polytypic phases coexist. Considering that various TMB_3 polytypes may coalesce in experimental samples, a large supercell is needed to model the coexistence of multiple polytypic phases. We construct a 50-metal-layer supercell with randomly stacked metal layers. Comparisons between our simulated XRD patterns and the experimental data[28, 32] are displayed in Fig. 7. As discussed above, the strong antibonding interaction in $hP3$-TMB_2 brings about an increase in the c-axial lattice constant, resulting in a significant mismatch between the simulated and experimental XRD patterns. The simulated XRD patterns for the polytypic TMB_3 phases, on the other hand, agree well with the experiments. In fact, our results reproduce well all seven high-intensity peaks observed in experiments. The reason that the seven major diffraction peaks are not affected by the random stacking is that they correspond to the underlying periodicity of all TMB_3 polytypes, which can be viewed as "metal-deficient" $hP3$-TMB_2 phases. Random stacking of metal layers does not change the lattice framework of the $hP3$ structure and the distances between crystal planes. Therefore, these results provide clear evidence that the long assumed $hP3$-TMB_2 phases should in fact be the TMB_3 polytypes identified here. We would like to mention that in experimental samples, the voids created by metal vacancies are large enough to accommodate interstitial boron atoms. The presence of interstitial boron atoms may be common among this type of crystals,[15,

[48] but we did not investigate this non-stoichiometric possibility.

Finally, we briefly discuss the high potential of this family of polytypes in designing novel superhard materials with additional functionalities. According to the above estimated hardness, each WB_3 polytype is only hard but not superhard since the interlayer W-B bonds largely limit the intrinsic hardness. It was verified by the theoretical study of *hP*16-WB_3 that has the lowest indentation shear strength along the [110] direction under the (001) plane.[65] If the relatively easy sliding between layers can be suppressed, the hardness will enhance greatly. This can be achieved by synthesizing a multiphase solid-solution nanocomposite material with the coexistence of various polytypes. This material includes a large number of interfaces among different polytypic structures with different easy sliding directions, and these interfaces will strongly hinder the interlayer sliding movement of each polytype, accordingly enhancing the extrinsic hardness. This extrinsic hardening mechanism, together with the intrinsic high hardness of each WB_3 polytype, well explains the superhardness (49.8±3.6 GPa) of the claimed AlB_2-type WB_2 nanocomposite sample (in fact the WB_3 polytypes).[28] As a matter of fact, the ultrahigh hardness of the recently synthesized nanotwin *c*BN and diamond samples[66, 67] has also corroborated this hardening mechanism. Compared with traditional solid-solution hardening by different compositional compounds, this hardening way by creating a polytypic multiphase does not change the chemical composition of materials. Moreover, this type of polytypic nanocomposite materials may be synthesized more easily since these different polytypes are energetically degenerate. Even these superhard polytypes exhibit anomalously low lattice thermal conductivity due to structural disorders and phonon folding, in contrast to the conventional knowledge that intrinsically strong chemical bonds in superhard materials should lead to high lattice thermal conductivity.[52] Therefore, the discovery of these polytypic structures promises to provide a new avenue to designing novel superhard materials with additional functionalities.

4 Conclusions

In summary, we have carried out a systematic investigation of the structural, energetic, and dynamical properties of the W-B and Mo-B systems using first-principles methods. Our results show that the *hP*3-TMB_2 phases are energetically unfavorable and dynamically unstable, and their calculated structural parameters, mechanical properties and XRD deviate significantly from experiments. In contrast, the TMB_3 polytypes are energetically more favorable and dynamically stable, and their corresponding properties agree well with experiments. We thus conclude that the long perceived *hP*3-TMB_2 phases are actually a misassignment for a family of more complex TMB_3 polytypes with a nanoscale ordering along the axial direction. More importantly, we demonstrate that such a structural and compositional modification is a consequence of relieving the strong antibonding interaction in the ideal *hP*3 structure. Therefore, the present work not only resolves several longstanding puzzles regarding structural and mechanical properties of the W-B and Mo-B systems, but also corroborates the existence of a family of polytypes. Our findings provide a new avenue for designing superhard nanocomposite materials with novel functionalities.

Acknowledgements

We acknowledge financial support from the Science and Technology Commission of Shanghai Municipality (Grant No.13JC1402900, 14XD1424300) and the State Oceanic Administration (No.SHME2013JS01). P.Z. acknowledges the support from the U.S. NSF under Grant DMR-0946404 and DMR-1506669, NSFC (Grant No. 11328401), and SUNY Networks of Excellence.

Notes and references

1 H. Y. Chung, M. B. Weinberger, J. B. Levine, A. Kavner, J. M. Yang, S. H. Tolbert and R B Kaner, *Science*, 2007, **316**, 436.

2 H. Jang, G. Friemel, J. Ollivier, A. V. Dukhnenko, N. Yu. Shitsevalova, V. B. Filipov, B. Keimer and D. S. Inosov, *Nat. Mater.*, 2014, **13**, 682.

3 M. Neupane, N. Alidoust, S. -Y. Xu, T. Kondo, Y. Ishida, D. J. Kim, Chang Liu, I. Belopolski, Y. J. Jo, T. -R. Chang, H. -T. Jeng, T. Durakiewicz, L. Balicas, H. Lin, A. Bansil, S. Shin, Z. Fisk and M. Z. Hasan, *Nat. Commun.*, 2013, **4**, 2991.

4 R. W. Cumberland, M. B. Weinberger, J. J. Gilman, S. M. Clark, S. H. Tolbert, R. B. Kaner, *J. Am. Chem. Soc.*, 2005, **127**, 7264.

5 J. Yang, H. Sun and C. Chen, *J. Am. Chem. Soc.*, 2008, **130**, 7200.

6 H. Niu, J. Wang, X. Q. Chen, D. Li, Y. Li, P. Lazar, R. Podloucky, and A. N. Kolmogorov, *Phys. Rev. B*, 2012, **85**,144116.

7 K. Kotmool, T. Kaewmaraya, S. Chakrabory, J. Anversa, T. Bovornratanaraks, W. Luo, H. Gou, P. C. Piquini, T. W. Kang, H. Mao and R. Ahuja, *Proc. Natl. Acad. Sci. U.S.A.*, 2014, **111**, 17050.

8 A. Knappschneider, C. Litterscheid, N. C.; George, J. Brgoch, N. Wagner, J. Beck, J. A. Kurzman, R. Seshadri and B. Albert, *Angew. Chem. Int. Ed. Engl.*, 2014, **53**, 1684.

9 H. Niu, X. -Q. Chen, W. Ren, Q. Zhu, A. R. Oganov, D. Li, and Y. Li, *Phys. Chem. Chem. Phys.* 2014, **16**, 15866.

10 Y. Liang, X. Yuan, Y. Gao, W. Zhang and P. Zhang, *Phys. Rev. Lett.*, 2014, **113**, 176401.

11 A. N. Kolmogorov, S. Shah, E. R. Margine, A. F. Bialon, T. Hammerschmidt and R. Drautz, *Phys. Rev. Lett.*, 2010, **105**, 217003.

12 H. Gou, N. Dubrovinskaia, E. Bykova, A. A. Tsirlin, D. Kasinathan, W. Schnelle, A. Richter, M. Merlini, M. Hanfland, A. M. Abakumov, D. Batuk, G. Van Tendeloo, Y. Nakajima, A. N. Kolmogorov and L. Dubrovinsky, *Phys. Rev. Lett.*, 2013, **111**, 157002.

13 H. Weng, J. Zhao, Z. Wang, Z. Fang and X. Dai, *Phys. Rev. Lett.*, 2014, **112**, 016403.

14 A. R. Oganov, J. Chen, C. Gatti, Y. Ma, Y. Ma, C. W. Glass, Z. Liu, T. Yu, O. O. Kurakevych and V. L. Solozhenko, *Nature*, 2009, **457**, 863.

15 A. T. Lech, C. L. Turner, R. Mohammadi, S. H. Tolbert and R. B. Kaner, *Proc. Natl. Acad. Sci. U.S.A.*, 2015, **112**, 3223.

16 B. Aronsson, T. Lundström and S. Rundqvist, *Borides, Silicides, and Phosphide*, Methuen, London, 1965.

17 P. Vajeeston, P. Ravindran and R. Asokamani, *Phys. Rev. B*, 2001, **63**, 045115.

18 H. P. Woods, F. E. Wawner and B. G. Fox, *Science*, 1966, **151**, 75.

19 X. Q. Chen, C. L. Fu, M. Krcmar and G. S. Painter, *Phys. Rev. Lett.*, 2008, **100**, 196403.

20 E. Zhao, J. Meng, Y. Ma and Z. Wu, *Phys. Chem. Chem. Phys.*, 2010, **12**, 13158.

21 Y. Liang, X. Yuan and W. Zhang, *Phys. Rev. B*, 2011, **83**, 220102(R).

22 Q. Li, D. Zhou, W. Zheng, Y. Ma and C. Chen, *Phys. Rev. Lett.*, 2013**, 110**, 136403.

23 Y. Liang, Y. Gou, X. Yuan, Z. Zhong and W. Zhang, *Chem. Phys. Lett.*, 2013, **580**, 48.

24 X. Y. Cheng, X. Q. Chen, D. Z. Li and Y. Y. Li, *Acta Cryst.*, 2014, C**70**, 85.

25 A. G. Van Der Geest and A. N. Kolmogorov, *Calphad*, 2014, **46**, 184.

26 M. Frotscher, W. Klein, J. Bauer, C. M. Fang, J. F. Halet, A. Senyshyn, C. Baehtz and B. Z. Albert, *Anorg. Allg. Chem.*, 2007, **633**, 2626.

27 W. Hayami, A. Momozawa and S. Otani, S. *Inorg. Chem.*, 2013, **52**, 7573.

28 C. Jiang, Z. Pei, Y. Liu, J. Xiao, J. Gong and C. Sun, *Phys. Status Solidi A*, 2013, **210**, 1221.

29 C. L. Jiang, Z. L. Pei, Y. M. Liu, H. Lei, J. Gong and C. Sun, *Appl. Surf. Sci.*, 2014, **288**, 324.

30 E. Storms and B. Mueller, *J. Phys. Chem.*, 1977, **81**, 318.

31 H. Klesnar, T. L. Aselage, B. Morosin, G. H. Kwei and A. C. Lawson, *J. Alloys Compd*., 1996, **241**, 180.

32 K. Kudaka, K. Iizumi, T. Sasaki and S. Okada, *J. Alloys Compd.*, 2001, **315**, 104.

33 Q. Tao, X. Zhao, Y. Chen, J. Li, Q. Li, Y. Ma, J. Li, T. Cui, P. Zhu and X. Wang, *RSC Adv.*, 2013, **3**, 18317.

34 M. Zhang, H. Wang, H. Wang, T. Cui, Y. Ma, *J. Phys. Chem. C*, 2010, **114**, 6722-6725.

35 Y. Liang, X. Yuan, Z. Fu, Y. Li and Z. Zhong, *Appl. Phys. Lett.*, 2012, **101**, 181908.

36 Q. Gu, G. Krauss and W. Steurer, *Adv. Mater.*, 2008, **20**, 3620.

37 M. Wang, Y. Li, T. Cui, Y. Ma and G. Zou, *Appl. Phys. Lett.*, 2008, **93**, 101905.

38 R. Mohammadi, A. T. Lech, M. Xie, B. E. Weaver, M. T. Yeung, S. H. Tolbert and R. B. Kaner, *Proc. Natl. Acad. Sci. U.S.A.*, 2011, **108**, 10958.

39 J. V. Rau, A. Latini, R. Teghil, A. D. Bonis, M. Fosca, R. Caminiti and V. R. Albertini, *ACS Appl. Mater. Inter.*, 2011, **3**, 3738.

40 C. Liu, F. Peng, N. Tan, J. Liu, F. Li, J. Qina, J. Wang, Q. Wang and D. He, *High Pressure Res.*, 2011, **31**, 275.

41 M. Xie, R. Mohammadi, Z. Mao, M. M. Armentrout, A. Kavner, R. B. Kaner and S. H. Tolbert, *Phys. Rev. B*, 2012, **85**, 064118.

42 R. Mohammadi, M. Xie, A. T. Lech, C. L. Turner, A. Kavner, S. H. Tolbert and R. B. Kaner, *J. Am. Chem. Soc*., 2012, **134**, 20660.

43 L. Xiong, J. Liu, L. Bai, Y. Li, C. Lin, D. He, F. Peng and J. F. Lin, *J. Appl. Phys.*, 2013, **113**, 033505.

44 P. A. Romans and M. P. Krug, *Acta Cryst.*, 1966, **20**, 313.

45 H. Gou, Z. Li, L. Wang, J. Lian and Y. Wang, *AIP Adv.*, 2012, **2**, 012171.

46 R. F. Zhang, D. Legut, Z. J. Lin, Y. S. Zhao, H. K. Mao and S. Veprek, *Phys. Rev. Lett.*, 2012, **108**, 255502.

47 Y. Liang, Z. Fu, X. Yuan, S. Wang, Z. Zhong and W. Zhang, *Europhys. Lett.*, 2012, **98**, 66004.

48 X. Cheng, W. Zhang, X. Q. Chen, H. Niu, P. Liu, K. Du, G. Liu, D. Li, H. M. Cheng, H. Ye and Y. Li, *.Appl. Phys. Lett.*, 2013, **103**, 171903.

49 I. Zeiringer, P. Rogl, A. Grytsiv, J. Polt, E. Bauer and G. Giester, *J. Phase Equilib. Diff.*, 2014, **35**, 384.

50 Q. Tao, D. Zheng, X. Zhao, Y. Chen, Q. Li, Q. Li, C. Wang, T. Cui, Y. Ma, X. Wang and P. Zhu, *Chem. Mater.* 2014, **26**, 5297.

51 T. Lundstrom and I. Rosenberg, *J. Solid State Chem.*, 1973, **6**, 299.

52 Y. Liang, J. Yang, X. Yuan, W. Qiu, Z. Zhong, J. Yang and W. Zhang, *Sci. Rep.*, 2014, **4**, 5063.

53 G. Kresse and J. Furthmuller, *Phys. Rev. B*, 1996, **54**, 11169.

54 J. P. Perdew, K. Burke and M. Ernzerhof, *Phys. Rev. Lett.*, 1996, **77**, 3865.

55 A. Togo, F. Oba and I. Tanaka, *Phys. Rev. B*, 2008, **78**, 134106.

56 R. Hill, *Proc. Phys. Soc. A*, 1952, **65**, 349.

57 X. Q. Chen, H. Niu, D. Li and Y. Li, *Intermetallics*, 2011, **19**, 1275.

58 H. Niu, X. Q. Chen, P. Liu, W. Xing, X. Cheng, D. Li and Y. Li, *Sci. Rep.*, 2012, **2**, 718.

59 P. Liu, F. Peng, S. Yin, F. Liu, Q. Wang, X. Zhu, P. Wang, J. Liu and D. He, *J. Appl. Phys.*, 2014, **115**, 163502.

60 J. K. Burdett, E. Canadell and G. J. Miller, *J. Am. Chem. Soc.*, 1986, **108**, 6561.

61 L. Topor and O. Kleppa, *J. Chem. Thermodyn.*, 1985, **17**, 1003.

62 A. F. Guillermet and G. J. Grimvall, *J. Less-Common Met.*, 1991, **169**, 257.

63 G. C. Trigunayat and G. K. Chadha, *Phys. Stat. Sol. A*, 1971, **4**, 9.

64 Y. Liang and B. Zhang, *Phys. Rev. B*, 2007, **76**, 132101.

65 C. Zang, H. Sun and C Chen, *Phys. Rev. B*, 2012, **86**, 180101(R).

66 Y. Tian, B. Xu, D. Yu, Y. Ma, Y. Wang, Y. Jiang, W. Hu, C. Tang, Y. Gao, K. Luo, Z. Zhao, L. M. Wang, B. Wen, J. He and Z. Liu, *Nature*, 2013, **493**, 385.

67 Q. Huang, D. Yu, B. Xu, W. Hu, Y. Ma, Y. Wang, Z. Zhao, B. Wen, J. He, Z. Liu and Y. Tian, *Nature*, 2014, **510**, 250.

Table 1 Structural and mechanical properties of the W-B and W-B systems. For the TMB_3 polytypes, the two basic structures, *hP*16 and *hR*24, are presented as representatives, and other polytypic phases are similar.

	WB_x				MoB_x			
	D_1 (Å)	D_2 (Å)	G(GPa)	H(GPa)	D_1 (Å)	D_2 (Å)	G(GPa)	H(GPa)
*hP*3 (calc.)	3.021	3.361	153	12.2	3.030	3.330	169	16.4
*hP*16 (calc.)	3.002	3.157	252	39.4	3.008	3.143	237	37.3
*hR*24 (calc.)	3.009	3.136	251	38.3	3.016	3.121	233	36.0
Expt.	3.02[a]	3.06[a]	249[b]	34.6-49.8[a]	3.043[c]	3.066[c]	-	15.2-27.0[d]

[a]Ref. 28, [b]Ref. 41, [c]Ref. 32, [d]Ref. 33.

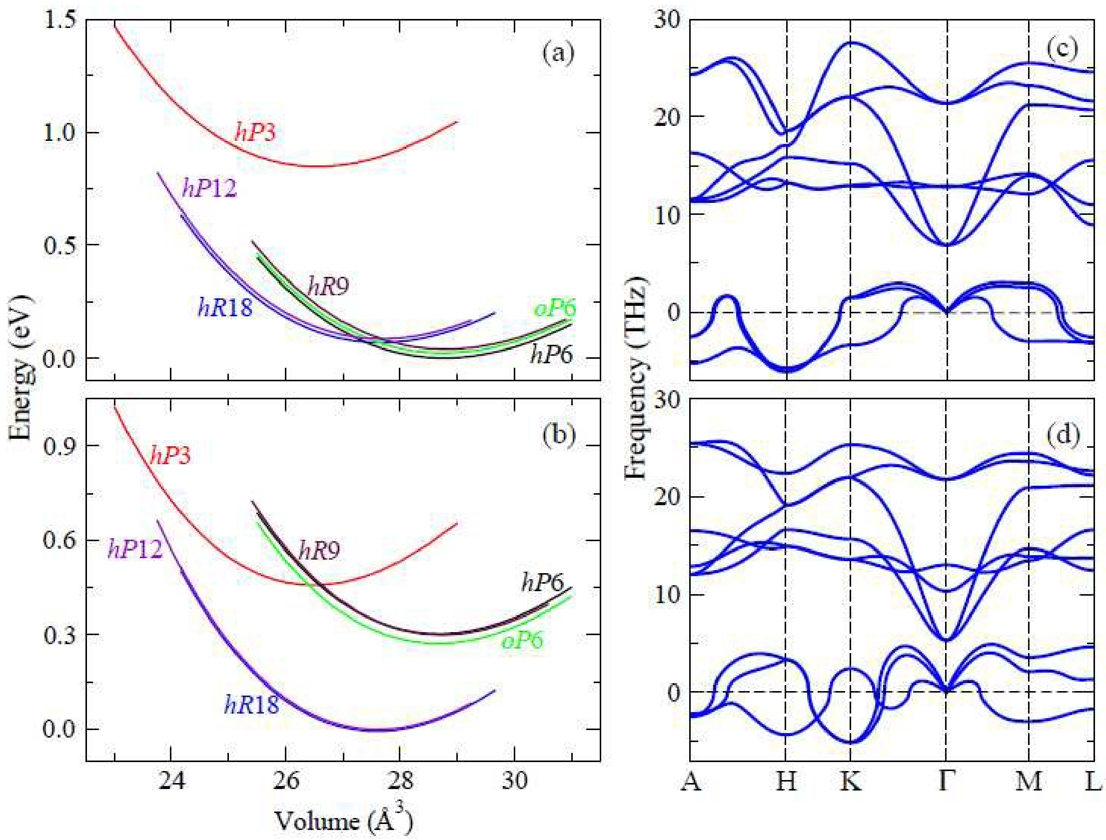

Fig. 1 Calculated total energies versus volumes for six candidate structures (*hP*3, *hP*6, *hP*12, *hR*18, *hR*9, and *oP*6) for (a) WB_2 and (b) MoB_2, and phonon dispersion curves of (c) WB_2 and d) MoB_2 with the *hP*3 structure. All energies are rescaled for one TMB_2 formula. It can be clearly seen that both *hP*3-WB_2 and *hP*3-MoB_2 are dynamically unstable due to the presence of imaginary phonon frequencies.

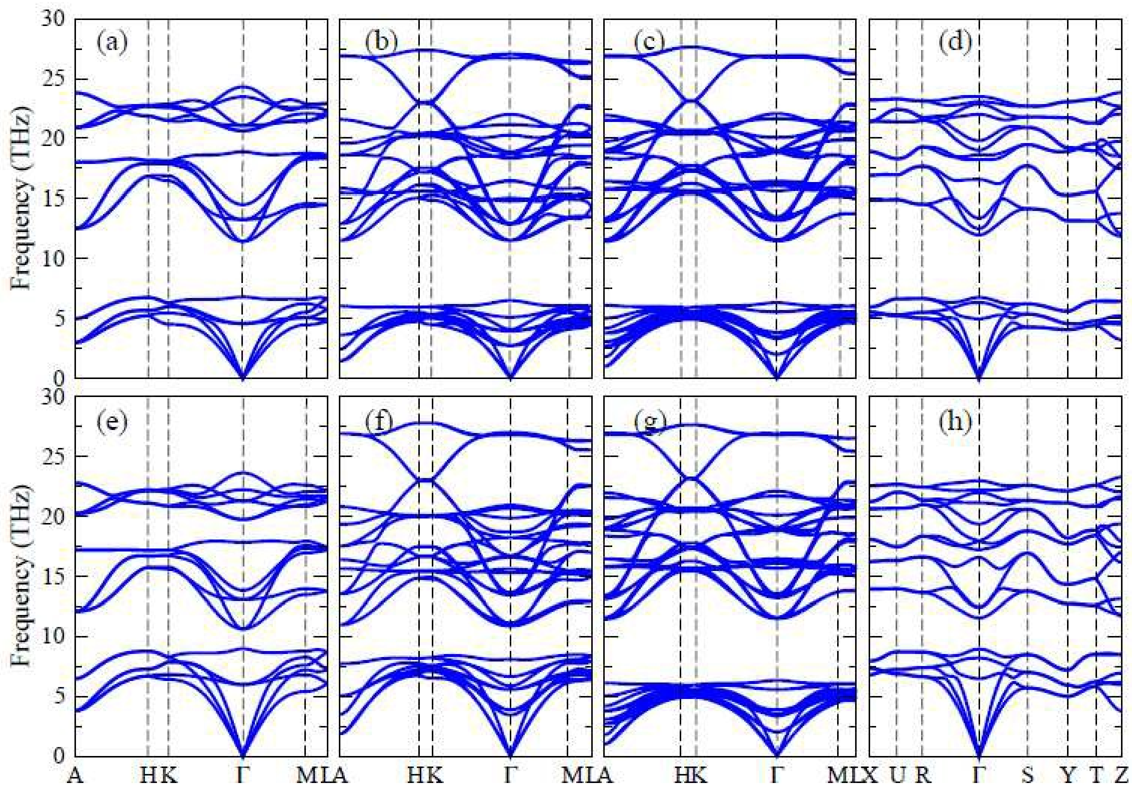

Fig. 2 Calculated phonon dispersion curves of the *hP*6, *hP*12, *hR*18, and *oP*6 structures (from left to right) for WB_2 (top panels) and MoB_2 (bottom panels). It can be clearly seen that these eight phases are all dynamically stable because no imaginary frequencies are observed. Phonon dispersion curves of the *hR*9 structure are shown in Ref. 24 and thus are not given here.

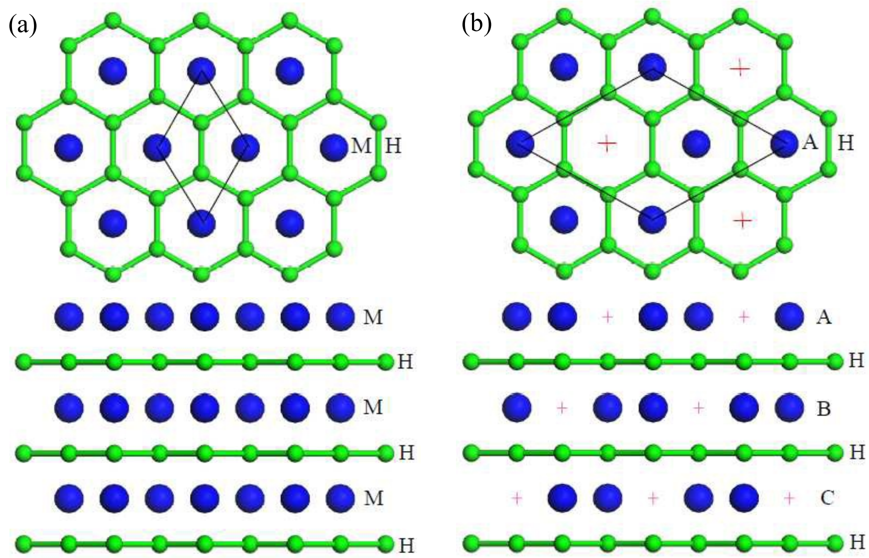

Fig. 3 Top and side views of boron (H) and metal (M, A, B, C) layers for (a) the *hP*3-TMB_2 phases and (b) the polytypic TMB_3 phases. The metal-deficient A layer can be derived from the close-packed M layer by removing one third of the metal atoms (marked by the red plus sign "+") methodically, and the B and C layers are actually the A layer displaced by one and two metal atoms, respectively. The black solid lines denote the unit cell of each phase. The small (green) and large (blue) spheres represent the boron and metal atoms, respectively.

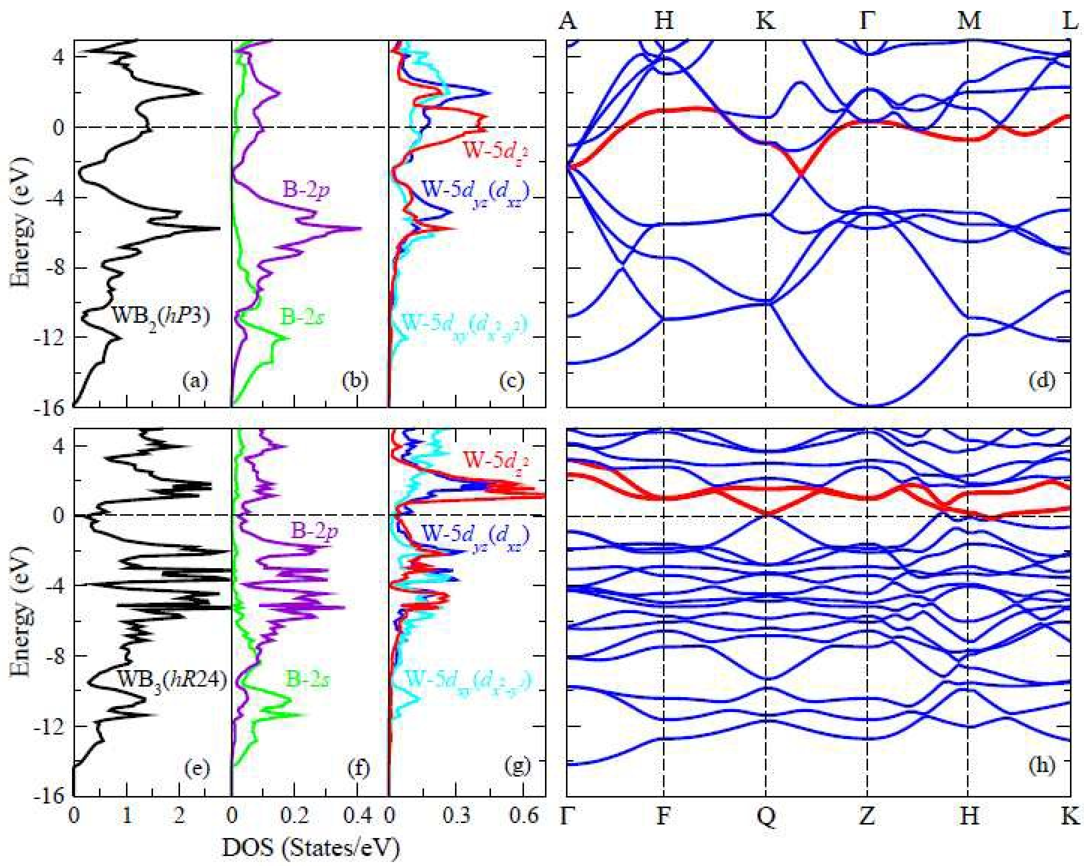

Fig. 4 Total, B-projected and W-projected DOS and band structures (from left to right) of the *hP*3-WB_2 phase (top panels) and the *hR*24-WB_3 phase (bottom panels). The Fermi levels are set at 0 eV and shown as horizontal dashed lines.

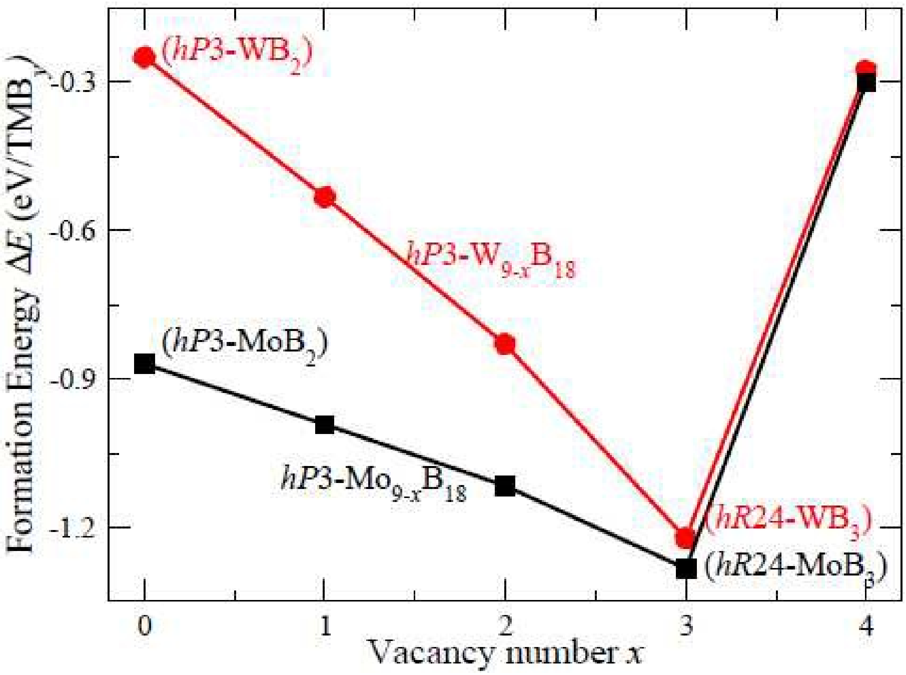

Fig. 5 Formation energies for *hP*3-TMB_2 as a function of the vacancy number. A ($\sqrt{3}\times\sqrt{3}\times 3$) supercell of the *hP*3 structure (i.e., *hP*3-$TM_{9\text{-}x}B_{18}$) is adopted and all formation energies are rescaled for one TMB_y formula.

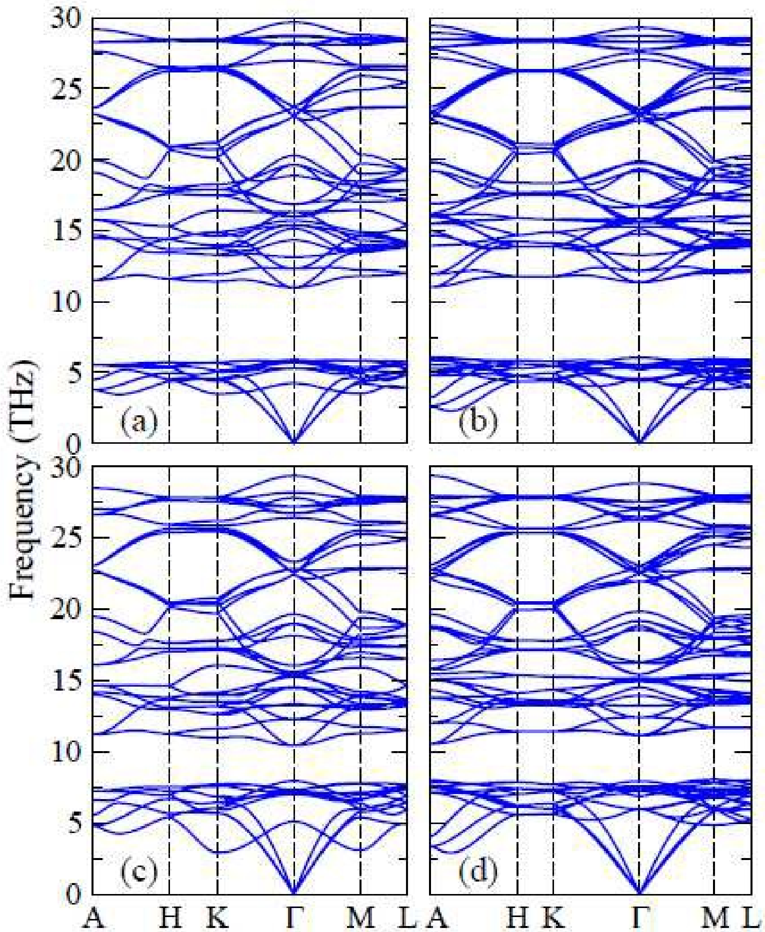

Fig. 6 Calculated phonon dispersion curves of the (a) *hP*16-WB_3, (b) *hR*24-WB_3, (c) *hP*16-MoB_3, and (d) *hR*24-MoB_3 phases. It can clearly see that the four phases are all dynamically stable because no imaginary frequencies are observed.

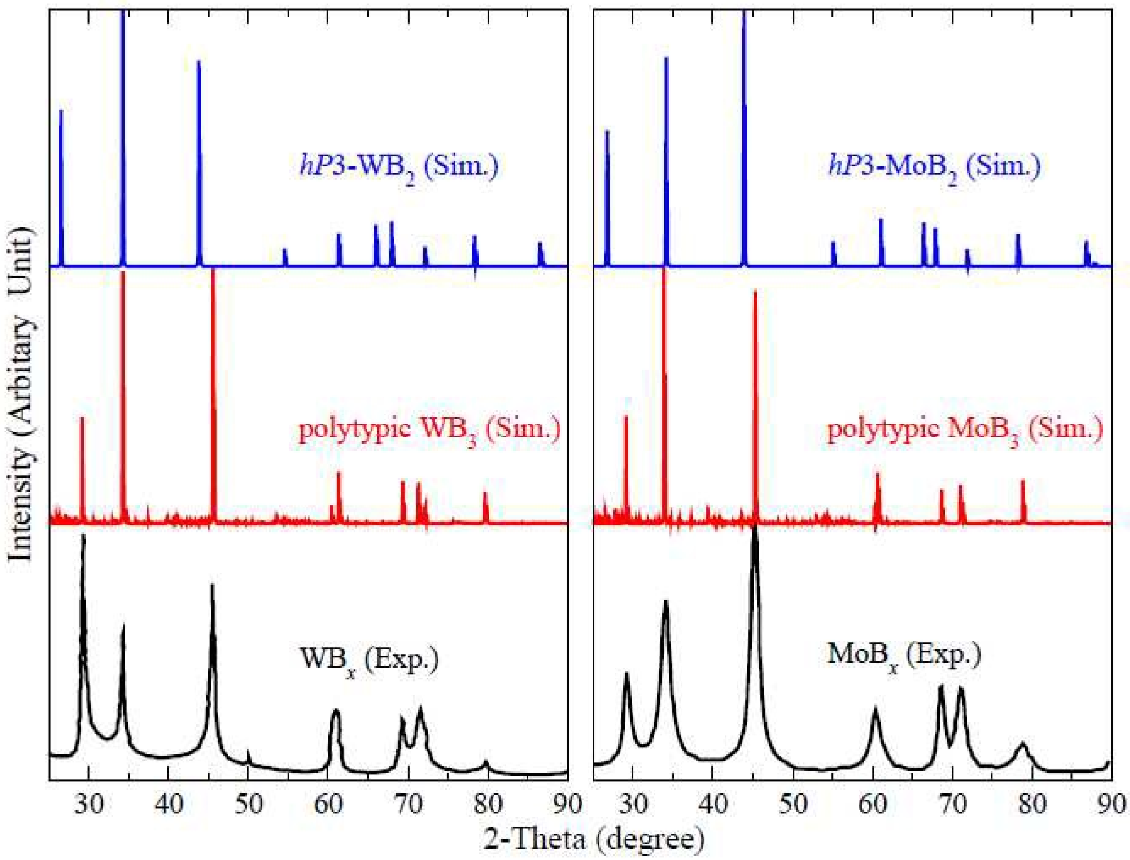

Fig. 7 Simulated XRD patterns of *hP*3-TMB_2 and polytypic TMB_3 supercells. The TMB_3 supercells include 50 metal layers with random stacking sequences to imitate the coexistence of multiple TMB_3 polytypes. For comparison, the experimental XRD patterns of WB_x and MoB_x are reproduced from Ref. 28 and Ref. 32, respectively.